



HAL
open science

Evaluating the Impact of Domain Boundaries on Hemodynamics in Intracranial Aneurysms within the Circle of Willis

Pablo Jeken-Rico, Aurèle Goetz, Philippe Meliga, Aurélien Larcher, Yigit Özpeynirci, Elie Hachem

► **To cite this version:**

Pablo Jeken-Rico, Aurèle Goetz, Philippe Meliga, Aurélien Larcher, Yigit Özpeynirci, et al.. Evaluating the Impact of Domain Boundaries on Hemodynamics in Intracranial Aneurysms within the Circle of Willis. *Fluids*, 2023, Image-Based Computational and Experimental Biomedical Flows, 9 (1), pp.1-10.3390/fluids9010001 . hal-04379043

HAL Id: hal-04379043

<https://hal.science/hal-04379043v1>

Submitted on 23 Oct 2024


HAL is a multi-disciplinary open access archive for the deposit and dissemination of scientific research documents, whether they are published or not. The documents may come from teaching and research institutions in France or abroad, or from public or private research centers.

L'archive ouverte pluridisciplinaire **HAL**, est destinée au dépôt et à la diffusion de documents scientifiques de niveau recherche, publiés ou non, émanant des établissements d'enseignement et de recherche français ou étrangers, des laboratoires publics ou privés.



Distributed under a Creative Commons Attribution 4.0 International License

Evaluating the Impact of Domain Boundaries on Hemodynamics in Intracranial Aneurysms within the Circle of Willis

Pablo Jeken-Rico ¹ , Aurèle Goetz ¹, Philippe Meliga ¹, Aurélien Larcher ¹, Yigit Özpeynirci ², Elie Hachem ^{1*}

¹ Computing and Fluids Research Group, Mines Paris, Université PSL, Centre de Mise en Forme des Matériaux (CEMEF), UMR7635 CNRS, 06904 Sophia Antipolis, France; pablo.jeken_rico@minesparis.psl.eu, aurele.goetz@minesparis.psl.eu, philippe.meliga@minesparis.psl.eu, aurelien.larcher@minesparis.psl.eu

² Institute of Neuroradiology, University Hospital LMU Munich, Munich, 81377, Bavaria, Germany

* Correspondence: elie.hachem@minesparis.psl.eu

Abstract: Hemodynamic simulations are increasingly used to study vascular diseases like Intracranial Aneurysms (IA) and to further develop treatment options. However, due to limited data, some aspects must rely on heuristics, especially at the simulation's distal ends. In literature, Murray's Law is often used to model the outflow split based on vessel cross-section area, but this poses challenges for the communicating arteries in the Circle of Willis (CoW). In this study, we contribute by assessing the impact of Murray's Law in patient-specific geometries featuring IA at the posterior communication. We simulate different domain extensions, representing common modelling choices. We establish Full CoW simulations as a baseline to evaluate the effect of these modelling assumptions on hemodynamic indicators, focusing on IA growth and rupture-related factors like Wall Shear Stress (WSS) and Oscillatory Shear Index (OSI). Our findings reveal qualitative alterations in hemodynamics when not modeling posterior communication. Comparisons between computing the anterior circulation and computing the whole Circle of Willis reveal quantitative changes in WSS may reach up to 80%, highlighting the significance of modelling choices in assessing IA risks and treatment strategies.

Keywords: Computational hemodynamics; Intracranial aneurysms; Circle of Willis; Wall shear stress; Boundary conditions

1. Introduction

Intracranial Aneurysms (IA) are estimated to affect about 3.2% of the adult population. While the annual risk of rupture is moderate at 2.2%, they impose a significant burden on patients, physicians, and the healthcare system [1,2]. To prevent ruptures, considerable effort is invested in early diagnosis, growth prediction, and treatment of IA. Advances in non-invasive imaging techniques, such as Magnetic Resonance Angiography (MRA), have made regular preventive screenings increasingly feasible. Detecting IA at an early stage provides neuroradiologists with the opportunity to weigh treatment options or continue monitoring the aneurysm's evolution. In this decision process, physicians rely on the geometrical and topological characterization of the IA along with other patient records. While scoring methods based on statistics, like the PHASES score, may contribute to the decision-making process, they have been shown to be weak overall predictors [3].

Instead of relying solely on statistics, Computational Fluid Mechanics (CFD) is proposed as a promising complementary tool. The goal is to simulate the hemodynamics of IA and extract risk indicators to assess the severity of the case and potentially predict a rupture site. Despite substantial progress in this field [4–7], a latent dissent exists in the research community, highlighted during numerous CFD challenges. It was confirmed that due to various modeling strategies, participating teams obtained dissimilar results that, in some cases, could point towards different interpretations [8–11]. For a consolidated use of CFD in IA research, it is imperative to address open modeling questions in advance [12].

Citation: Jeken-Rico, P.; Goetz, A.; Özpeynirci, Y.; Meliga, P.; Larcher, A.; Hachem, E. Evaluating the Impact of Domain Boundaries on Hemodynamics in Intracranial Aneurysms within the Circle of Willis. *Fluids* **2023**, *1*, 0. <https://doi.org/>

Received:

Revised:

Accepted:

Published:

Copyright: © 2024 by the authors. Submitted to *Fluids* for possible open access publication under the terms and conditions of the Creative Commons Attribution (CC BY) license (<https://creativecommons.org/licenses/by/4.0/>).

Outflow Boundary Conditions (BCs) represent one recurring source of uncertainty in vascular fluid dynamics. Reliable measurements are challenging to obtain and are therefore rarely employed [12]. Instead, the Principle of Minimum Work can be used to prescribe the flow split among the distal ends of the simulated network based on the relationship of their cross-sectional areas [13]. This heuristic, arising from the pursuit of minimizing the energy spent on the transport and storage of blood, has been confirmed through ex-vivo analysis by analyzing the regularity of arterial branching patterns [14]. The Law of Minimum Work, also known as Murray's law, is not only more realistic than plain stress-free outflows [15,16] but also offers the advantage that it solely depends on the geometrical features of the network. This is advantageous as it makes boundary conditions reproducible across varying modeling assumptions, such as rheology laws, solver schemes, or boundary extrusions.

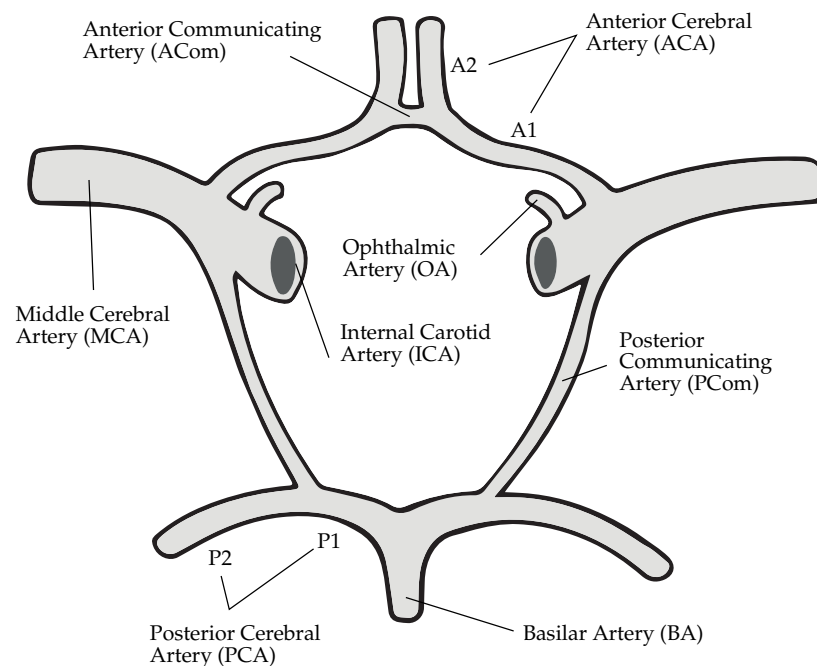


Figure 1. Schematic view of a complete CoW and the ophthalmic arteries.

Nevertheless, Murray's law has an unstudied implication when applied to the communicating arteries in the Circle of Willis (CoW), a loop of arteries found at the base of the brain (see Fig. 1). From an anatomical point of view, these vessels serve the purpose of linking anterior and posterior circulations, thereby providing alternative pathways for the blood in case of ischemia [17]. Frequently, the PCom carries a lesser net flow from the ICA to the PCA, albeit different CoW configurations may perturb this rule [18–20]. The majority of CFD studies that examine IA at the carotid arteries only consider one part of the anterior circulation, thereby defining the PCom as a regular system outlet [15,21] or neglecting it [22,23]. These two strategies pose two extreme cases and therefore inevitably raise the question, of whether they lead to physiological conditions or not.

The uncertainty surrounding the simulation domain of IA and the uncertainty in treating the PCom artery in CFD, as per existing literature, underscores the motivation for this study. Our aim is to evaluate changes in intra-aneurysmal hemodynamics in ICA-PCom bifurcation aneurysms by varying the extent of the simulated vasculature. These extensions are selected based on common observations from IA literature and are compared with full CoW simulations. The primary focus of the comparison lies in intra-aneurysmal flow patterns and the exposure of the lumen to shear stresses.

2. Materials & Methods

2.1. Medical Imaging and Segmentation

The angiography images were obtained using time-of-flight angiography on 1.5T and 3T MRI scanners with isotropic imaging and 0.6mm slice thickness. The lumen was segmented using [3DSlicer](#) under the supervision of neuroradiologists of the cooperating medical institution. Patient A has a complete CoW with one aneurysm of diameter 7.5 mm at the left ICA-PCoM bifurcation. Patient B has a bilateral P1 hypoplasia and is therefore missing a connection of the basilar artery with both anterior circulations. The PCoMs are defined in this case as fetal since their size is larger than usual and they are in fact the main supplier of blood to the PCA [24]. The aneurysm of the latter is located on the right side ($d = 5\text{ mm}$) and features a pronounced lateral daughter sack. The complex geometry of this formation was later confirmed with image recordings during the operation procedure. Lastly, patient C too has an incomplete CoW due to an absent right PCoM. In this case, two IA can be found, one at the left ICA-PCoM bifurcation and one at the right MCA bifurcation. The former, being the only one considered during analysis, is classified as bilobular, due to the presence of two rounded sacks.

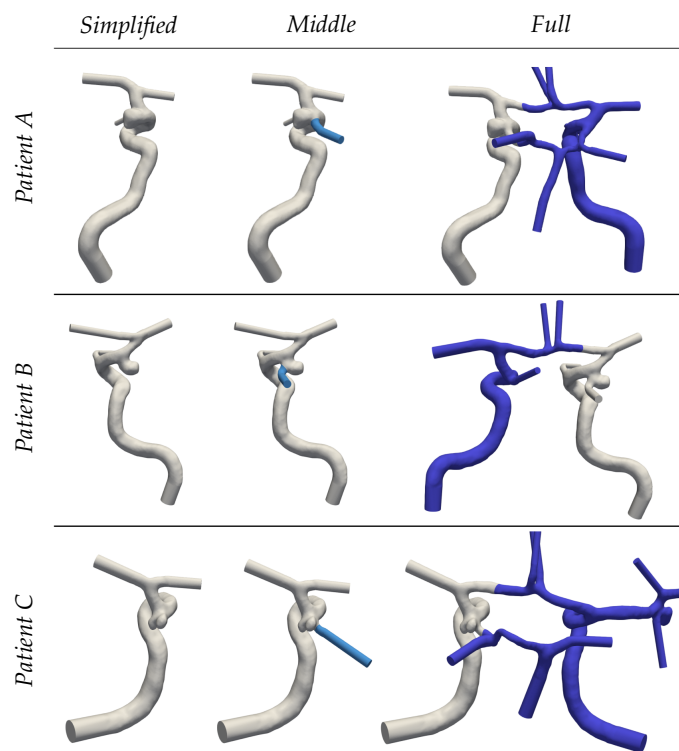


Figure 2. Overview of cases A-C (top to bottom) in the different extensions *Simplified-Full* (left to right). *Simplified* - Neglect of the adjacent PCoM. *Middle* - Simulation of ICA and proximal vessels. *Full* - Full computation of the CoW.

2.2. Spatial Discretization

For each of the segmented geometries, three extensions of ascending complexity (see Fig. 2) are generated to assess the implications of Murray's law on simulated hemodynamics. Geometries with the keyword *Simplified* are constrained to the main supplying artery that leads to the IA. Communicating arteries and A2 segments (see Fig. 1) are in this case neglected. *Middle* extends the prior *Simplified* complexity by adding the PCoM. Finally, the keyword *Full* denotes the full CoW. To minimize perturbations caused by inlet and outlet models, extrusions have been made along these boundary patches [12,22]. Circular profiles are adapted by a least-square fit to the irregular vessel cross-sections and extended along the mean vessel direction using transfinite interpolations. This procedure additionally

simplifies the imposition of circular inflow profiles and facilitates geometrical information required for the outflow boundary conditions.

The open 2D surface meshes are parametrized using conformal maps, remeshed and extruded inwards to generate a set of tetrahaedral boundary layers (growth factor 1.2) [25]. These boundary layers serve two crucial purposes in our fluid simulations of arteries. Firstly, the incorporation of boundary layers is essential for a more accurate resolution at the wall regions. Secondly, maintaining consistency in the structure at the boundaries permits comparison between different cases without disturbances of mesh-induced boundary effects. The layers' thickness is determined by the dimensionless wall distance of $y^+ = 1$, an overestimated Reynolds number of $Re = 1000$ and the averaged diameter of the ICAs. Based on a preliminary mesh convergence, and as proposed in [4], we fixed the mesh size $h = 0.2 \text{ mm}$ which is progressively refined to $h = 0.1 \text{ mm}$ at the aneurysm periphery (see Fig. 3), utilizing *gmsh*.

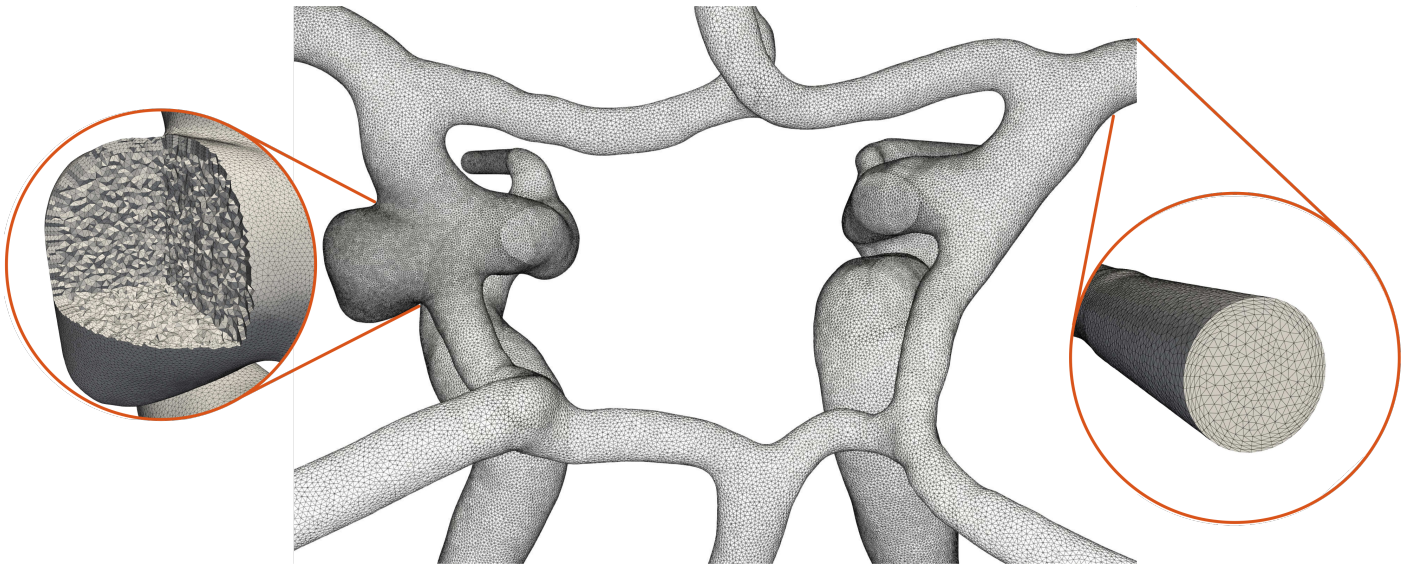


Figure 3. Visualization of the CoW of patient A with highlighted mesh features (orange circles). Linear isotropic refinement (left) and structured tetrahaedral boundary layers (right).

2.3. Hemodynamics Simulations

2.3.1. Navier-Stokes

The simulations have been carried out by numerically solving the transient, incompressible Navier-Stokes equations with an in-house Finite Element (FE) solver. The discrete system is set up by linear elements for both pressure and velocity and is consequently stabilized by a residual-based Variational Multiscale-type method [26,27]. The weak formulation (see Eqn. 1 and Eqn. 2) is enriched with the residuals of the continuity \mathcal{R}_C and residuals of momentum \mathcal{R}_M . For details on the stabilization parameters, τ_C and τ_M , we refer to [26] and therein. The time integration has been carried out with a second order semi-implicit backward scheme, which has shown to provide a good balance between memory and consistency [28,29].

$$\begin{aligned} & \int_{\Omega} \underbrace{\rho(\partial_t \vec{u}_h + (\vec{u}_h \cdot \nabla) \vec{u}_h) \cdot \vec{w} + \sigma : \nabla \vec{w}}_{\text{Galerkin terms}} d\Omega + \sum_{\Omega_e \in \Omega} \int_{\Omega_e} \underbrace{\tau_M \rho (\vec{u}_h \cdot \nabla) \vec{w} \cdot \mathcal{R}_M}_{\text{Upwind stabilization}} d\Omega \\ & + \sum_{\Omega_e \in \Omega} \int_{\Omega_e} \underbrace{\tau_C \mathcal{R}_C \rho \nabla \cdot \vec{w}}_{\text{Grad-div stabilization}} d\Omega = \int_{\Gamma_h} \underbrace{\vec{w} \cdot \sigma \cdot \vec{n}}_{\text{Boundary stress}} d\Gamma, \quad \forall \vec{w} \in H^1 \end{aligned} \quad (1)$$

$$\sum_{\Omega_e \in \Omega} \int_{\Omega_e} \underbrace{\tau_M \nabla q \cdot \mathcal{R}_M}_{\text{Pressure stabilization}} d\Omega + \int_{\Omega} \underbrace{q \nabla \cdot \vec{u}_h}_{\text{Galerkin term}} d\Omega = 0, \quad \forall q \in H^1 \quad (2)$$

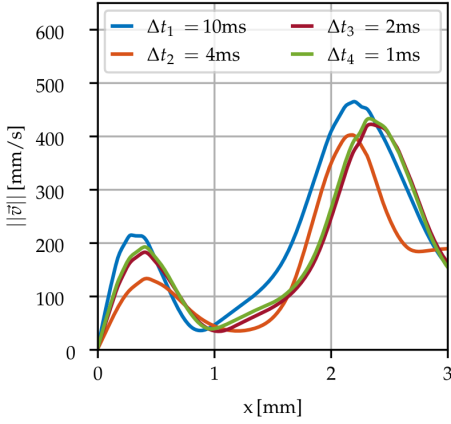


Figure 4. Velocity profile over aneurysm B for different time resolutions using described mesh.

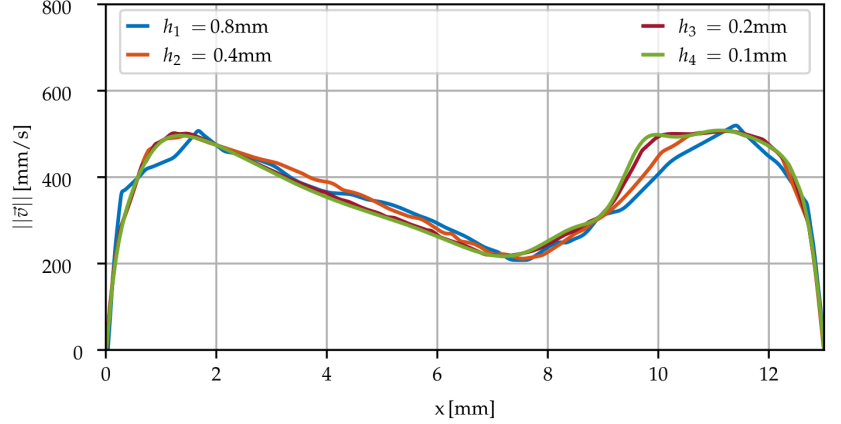


Figure 5. Velocity profile plotted over the C6-C7 ICA sections (Patient B) for different mesh sizes.

As mentioned previously, several benchmark validations with both space and time convergences analysis were made in [26,28] and more recently in the context of IA in [30]. The obtained parameters yielded stable simulations and match the proposed resolutions in IA-hemodynamics literature [4,23,31]. For completeness, we have added the effect of different timesteps and mesh resolutions (see Fig. 4 and Fig. 5) on a representative test case, patient B, allowing us to finally fix the time step to 1ms and the mesh size graduation from $h = 0.2 \text{ mm}$ to $h = 0.1 \text{ mm}$ at the aneurysm periphery for for all the simulations.

2.3.2. Rheology

The shear-thinning rheology is modelled through the Carreau model describing its behaviour [12,32,33] as in Eqn. (3). The constants $\rho = 1056 \text{ kg/m}^3$, $\mu_0 = 0.0456 \text{ Pa s}$, $\mu_\infty = 0.0032 \text{ Pa s}$, $\lambda = 10.03 \text{ s}$, $n = 0.344$ and the shear rate $\dot{\gamma}$ were employed [34].

$$\mu(\dot{\gamma}) = \mu_\infty + (\mu_0 - \mu_\infty) \left(1 + (\lambda \dot{\gamma})^2\right)^{(n-1)/2} \quad (3)$$

2.3.3. Boundary Conditions

Inflow conditions are described with the help of a generalized volumetric flow curve which has been scaled and split among the supplying arteries (see Fig. 6). More precisely, in case A each ICA contributes 44% of the total volumetric flow while the BA carries only 12% due to its small size [35]. Cases B and C follow a split of 40%-20% between each ICA and the BA. The flow rate Q is imposed via parabolic velocity profiles at the base of the arterial system. The walls are considered fully rigid and are thus set through no-slip conditions.

The outflow of the system follows Murray's Law, guiding flow distribution based on the cubed outlet radius, as expressed in Eqn. (4) [15,16]. The exponent three ($n=3$) aligns with Poiseuille flow assumptions on the long-term cost of blood transport in brain arteries [13]. This exponent has been chosen for consistency with the linear relationship $P = QR$ used to impose the desired flowrates. The rule is derived from fully established Poiseuille flow principles [36] and is commonly used in brain arteries [29,37]. Resistances R are adjusted iteratively for each outlet, ensuring a systematic application of Murray's Law across the system.

$$Q_{out,i}(t) = Q_{in}(t) \frac{r_i^3}{\sum_j r_j^3} \quad (4)$$

2.3.4. Computation Details

For the solution, the fully coupled system of pressure and velocity was solved in parallel using the ILU(4) block preconditioned Stabilized Bi-Conjugate Gradient method. The simulations were carried out on dual processors (32-Core AMD EPYC 64-bit Processor 7502, Advanced Micro Devices, Santa Clara, CA, USA) with a 2.5GHz base clock rate and a HDR 100 interconnection. Computing times of each cardiac cycle can be extracted from Table 1. The number of elements, likewise seen in Table 1, is notably higher for case A due to its larger volume and aneurysm sack.

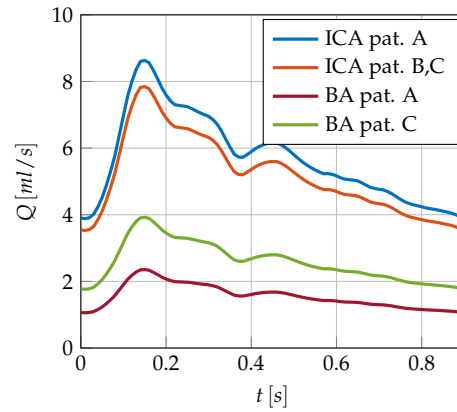


Figure 6. Volumetric inflow of patients A-C.

Patient		<i>Simplified</i>	<i>Middle</i>	<i>Full</i>
A	n_{elem}	3.4	3.8	7.1
	T_{comp}	9:20 h	10:12 h	22:10 h
B	n_{elem}	2.0	2.1	3.6
	T_{comp}	4:41 h	5:19 h	8:23 h
C	n_{elem}	1.6	1.7	4.7
	T_{comp}	5:07 h	5:46 h	8:30 h

Table 1. Element count in million elements and computation time per cardiac cycle of different meshes.

2.4. Hemodynamic Descriptors

The influence of different domain extensions is assessed through key hemodynamic indicators, including wall shear stress (WSS), oscillatory shear index (OSI), and velocity profiles. Velocity, being a primal variable, is inherently linked to any alterations in system dynamics and is therefore considered for initial assessments. WSS and OSI, belonging to a set of indicators related to vascular remodeling, are recognized as risk factors in aneurysm formation [38–40]. According to Meng et al. [41], destructive remodeling phenomena of arterial walls can be categorized into mural-cell-mediated events caused by abnormally high WSS and inflammatory remodeling induced by low WSS and high OSI. However, despite the identification of general trends in the literature [42], a consensus on threshold values for WSS and OSI in brain arteries remains elusive [43]. Recent advancements in hemodynamic research have introduced WSS-derived quantities, such as the WSS gradient topology [44] and the relative residence time (see [45] and therein). These novel indicators provide insights into the pulsatility and topological structure of WSS distributions. Recognizing the critical role of WSS in these advancements, our work primarily focuses on its accurate computation. These quantities are calculated from the velocity fields through the stress tensor σ as illustrated in Eqn. 5 and Eqn. 6, respectively.

$$\vec{\tau}_{wss} = \vec{n} \times (\sigma \cdot \vec{n}) \times \vec{n} \quad (5)$$

$$OSI = \frac{1}{2} \left(1 - \frac{\left\| \int_0^T \vec{\tau}_{wss} dt \right\|}{\int_0^T \|\vec{\tau}_{wss}\| dt} \right) \quad (6)$$

3. Results

3.1. Simulations

The overall flow distribution can be visually followed from the velocity magnitudes shown in Fig. 7. Patient A stands out due to slower flow velocities despite similar tributary flows, which is a direct consequence from having overall larger vessels compared to B

and C. The plot highlights regions of high flow speeds as for instance in the terminal ICA bifurcation. The highly inertia driven flow turns mostly into the MCAs, which both due to their size and the Murray exponent ($n=3$), carry the largest outflow. The BA, when present, supplies the posterior circulation of the brain without directly irrigating the anterior circulation. Therefore, the flux traversing the PCom is strictly unidirectional carrying blood away from the ICA towards the PCA, in accordance with the commonly observed flow direction [19,46]. Patient B and C feed, according to our models, the distal PCA mostly (Patient C) or exclusively (Patient B) through the PCom due to their small or fetal P1 segments.

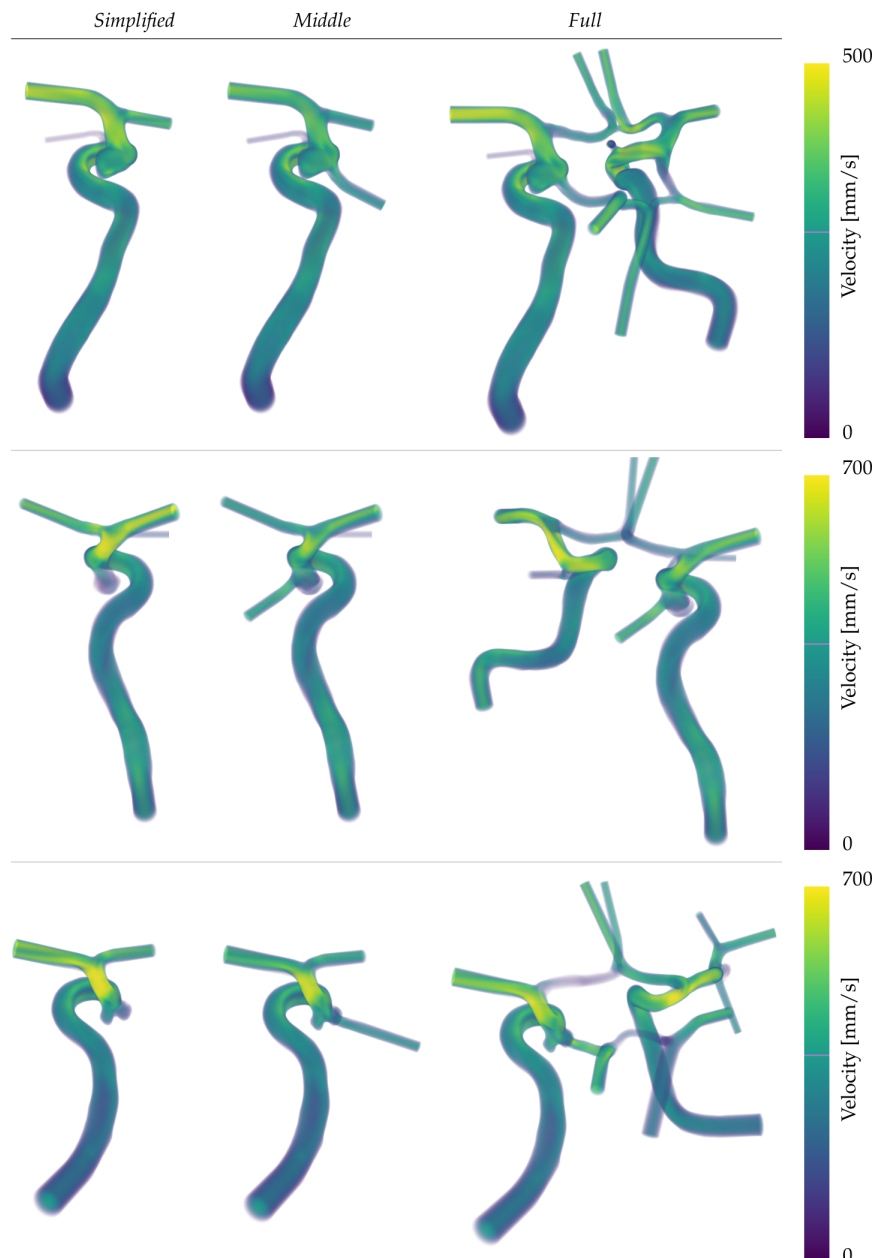


Figure 7. Maximum velocity projection of patients A-C (top to bottom) for all complexity levels *Simplified-Full* (left to right) at diastole.

The detailed presentation of the average blood transported through each vessel is provided in Table 2. Notably, in the *Full* configuration, the flow through the A2 segment of the ACA is consistently smaller, exhibiting a deviation of up to 5 percentage points compared to the *Middle* and *Simplified* configurations. The *Middle* configuration is characterized

by guiding flow away from the MCA towards the A1 segment of the ACA, representing a distinct pattern in the distribution of blood flow. These observations are relevant for the later discussion of the biases of Murray's law. Additionally, the volumetric flow has been recorded at the vessels close to the aneurysms. Fig. 8 shows this quantity normalized with respect to the maximum mean flow of the three extensions. It can be seen that in the *Simplified* simulations the flow that would leave through the PCom is distributed among the other outlets, causing their flow rates to be consistently higher. The *Middle* distinguishes itself from the *Full* through lower outflows through the MCA and larger ones through the ACA but exhibits no general trend on the PCom.

Case	Complexity	MCA		PCA		ACA		OA	
		Left	Right	Left	Right	Left	Right	Left	Right
A	<i>Full</i>	28.8%	25.7%	14.0%	7.7%	7.2%	9.3%	3.1%	4.2%
	<i>Middle</i>	21.8%	-	10.6%	-	9.2%	-	2.4%	-
	<i>Simplified</i>	28.8%	-	-	-	12.1%	-	3.1%	-
B	<i>Full</i>	29.3%	21.6%	4.9%	9.6%	4.3%	7.0%	-	3.1%
	<i>Middle</i>	-	20.9%	-	9.3%	-	6.8%	-	3.1%
	<i>Simplified</i>	-	27.2%	-	-	-	8.8%	-	4.0%
C	<i>Full</i>	27.1%	35.9%	12.0%	12.4%	4.0%	8.5%	-	-
	<i>Middle</i>	22.1%	-	7.5%	-	10.3%	-	-	-
	<i>Simplified</i>	27.3%	-	-	-	12.7%	-	-	-

Table 2. Outflow per cardiac cycle with respect to the in total inflow of each patient. In the *Large* configuration of case C, the flow in the right MCA was the consequence of imposing Murray's law on the vessels of the M1-M2 bifurcation. The massflow for the *Middle* and *Small* is taken at the A1 ACA segment due to the inherent cut of the domain.

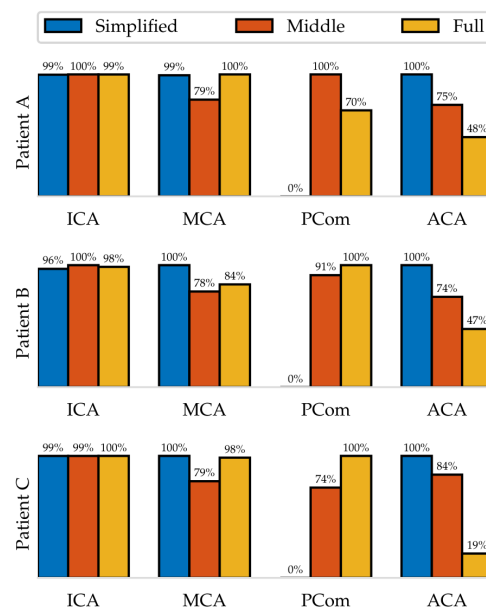


Figure 8. Mean volumetric flow per cardiac cycle in the IA proximity. The percentage values describe how much flow with respect to the other configurations passes through the indicated vessel. The cuts of the MCA and ACA are set at the M1 and A1 segments, respectively.

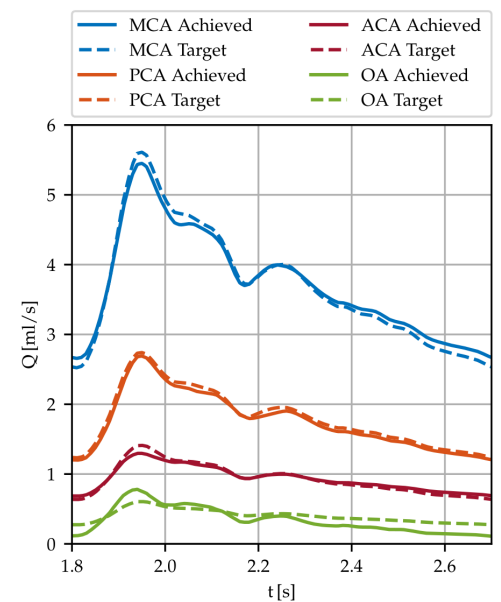


Figure 9. Volumetric flow through the left ICA outlets of patient A comparing the targeted (dashed lines) flow as dictated by Murray's Law (see Eqn. (4)) values with the obtained ones using the linear pressure relationship $P = QR$ after fitting the resistances.

For verification purposes, the goodness of the boundary condition model is shown for which the resistances R_i have been fitted in an iterative process to minimize L_1 error between the targeted flow and the achieved one. In Fig. 9 the volumetric flow of the left hemisphere's outlets (aneurysm A) are shown together with the targeted curves as a

representative example of the fitting performance. The linear law enables controlling the mass flow through pressure BCs within a relative error of 5% per cardiac cycle despite non-Newtonian and transient flows. The largest relative deviations have been observed at small vessels during peak systolic and peak diastolic times, as for instance the OA (green curves) in Fig. 9.

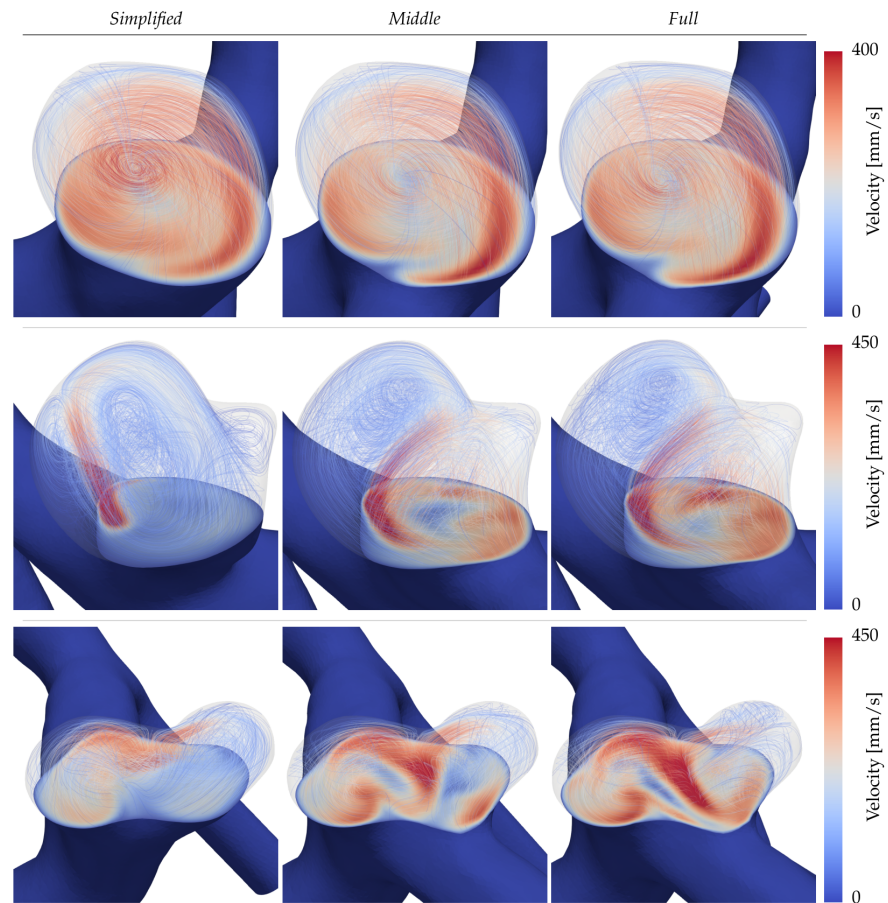


Figure 10. Cross-section cuts at the IA neck of patients A-C (top to bottom) with inscribed velocity magnitudes at diastole. Velocity streamlines are superposed with the aneurysm necks to highlight the structure of the flow.

3.2. Intra-aneurysmal Dynamics

The flow structures in the domes are visualized in Fig. 10 for each patient (rows) and configuration (columns). The aneurysms are cut with a plane at the neck and velocity streamlines of the intra-aneurysmal flow are inscribed lightly to indicate the structure of the present vortices at peak diastolic time. For the inertial flow of aneurysm A (first row), all three configurations show a large, centred vortex traversing the dome that can be regarded as consistent across the three sizes. Per contrary, patients B and C in the second and third rows of Fig. 10 display clear discrepancies. Starting with the aneurysm B (second row) it is visible that in the simple configuration, the main inflow enters the dome focused as a small jet, later decaying into a stable weaker recirculation. For the *Middle* and *Full* extensions of the same case, the inflow hits the neck of the daughter sack, splitting its momentum among two vortices that traverse the main lobe and the daughter sack respectively. In the *Full* simulation of B (second row, third column) the daughter sack's recirculation is located farther up inside the dome leading to larger in-plane velocities. Lastly, patient C (third row of Fig. 10) presents the largest disparities on both quantitative and qualitative levels. One of the most noticeable differences in Fig. 10, is the inverted circulation of the right aneurysm

dome in the *Full* simulation with respect to the other two extensions. At the same time, the impinging jet's velocities exceed the other cases by on average 31% and 19%.

3.3. Wall Shear Stress

The WSS magnitude for peak diastole and systole are shown in Fig. 11 a) and b) respectively. Patient A (first row) is characterized by a stable, qualitatively similar WSS pattern across all extensions. Here, only the *Simplified* case demonstrates smaller patches of higher shearing that are not present in the *Middle* and *Full* systems. Patients B and C instead exhibit persistently altered WSS patterns for all of the domain extensions. Setting the *Simplified* system aside, one can observe shifts in patterns between the *Middle* and *Full* extensions in the second and third columns respectively. Most notable here is the daughter sack in patient B's aneurysm (second row of Fig. 11). During diastole, the WSS is relatable between the *Middle* and *Full* systems. At systole, on the contrary, the shearing increases for the *Middle* system, but remains low for the *Full* system, leading to two distinct characterizations. Following the *Full* system, the daughter sack could be identified as a risk factor due to low WSS exposure, whereas the *Middle* simulation would not. Daughter sacks play hereby an important role since their appearance is linked to an augmented risk of rupture. The last patient case in the bottom row of Fig. 11 a) and b), again shows an inconsistent WSS among the different extensions, especially aggravated at the dent separating the two sacks.

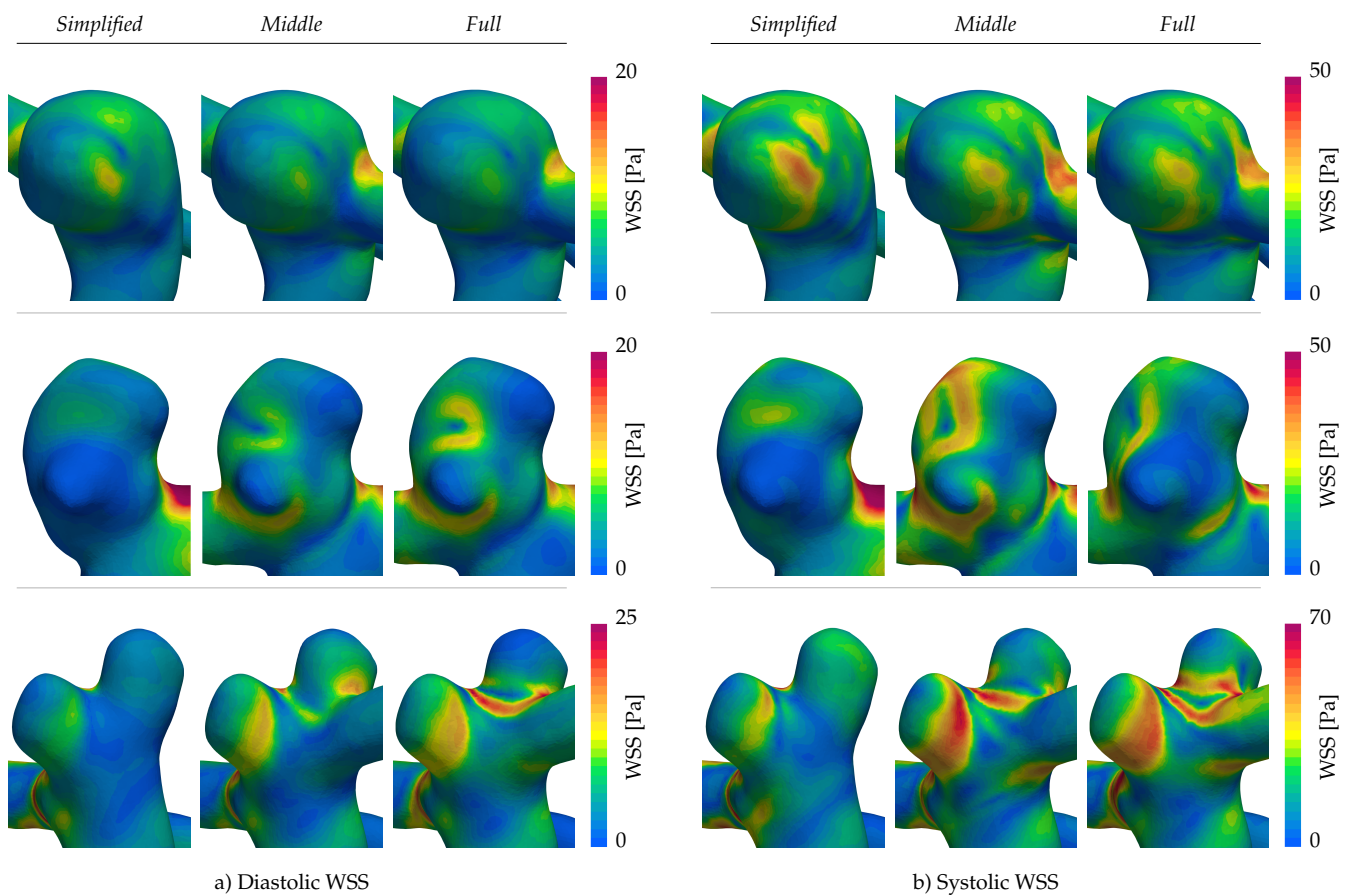


Figure 11. WSS distributions on the aneurysms A-C (top to bottom) for the different complexity levels at diastole (a) and peak systole (b).

3.4. Oscillatory Shearing

Following the same structure of Fig. 11 a) and b), the OSI is displayed in Fig. 12. The observed stable WSS profile of aneurysm A inevitably leads to a nearly absent oscillatory

shearing with only small localized peaks (see the first row in Fig. 12). Large dissent of the OSI distributions is again found in patients B and C (second and third rows of Fig. 12), where especially the distal lobe of patient C points out. There, overall high values are found on the visible face in the *Full* CoW simulation, in contrast to the other cases.

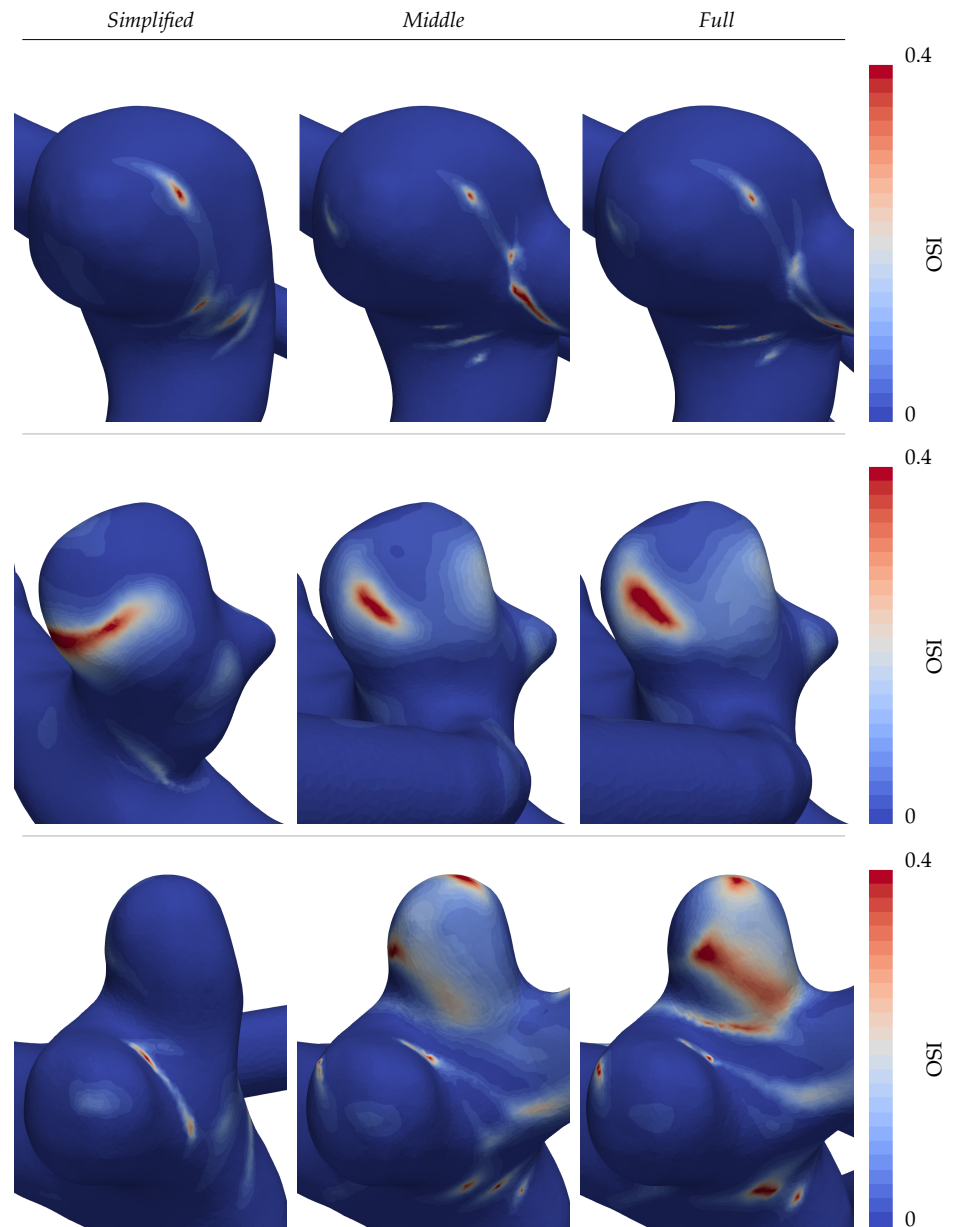


Figure 12. OSI distributions for cases A-C (top to bottom) under different geometry extensions.

4. Discussion

The results have shown a satisfactory application of resistive boundary conditions to the simulation of hemodynamics, providing accuracies of above 95% with respect to the targeted flows of Murray's law. The resulting flow in the CoW resembles literature values [47] with a tendency to overestimate the flow through the MCAs. Using an exponent of ($n=2$) in Murray's law (see Eqn.(4)) reduces the discrepancy for the flow in the MCA at the cost of overestimating the flows in smaller vessels, such as the OA. Detailed measurements of brain arterial trees [14] suggests that Murray's law is best fit by exponents that grow from two in the proximal sections towards 3 in the more distal sections. While this is a factor is important to consider in general, we opted for a consistent modelling of the distal

systems based on the Poiseuille flow. For a more detailed analysis of this matter we refer to [16] and [21], which study the different exponents, area estimations and bifurcation rules in relationship with Murray's law.

The changes in the flow through the ACA between the different computational domain extensions are a direct consequence of Murray's law being applied on vessels of varying diameter. The proximal ACA (A1) has, in all cases, a larger radius than its post-communicating segment (A2), consequently leading to different flow rates according to Eqn. (4). However, this apparent inconsistency is caused by perforator vessels around the ACom, such as the Recurrent Artery of Heubner, which, due to their small size, cannot be properly simulated. Experimental studies [47] support the observed decrease in flow rates. In our cases, applying Murray's law has shown a better agreement in ACA and MCA flowrates with the said study when setting the domain boundary in the A1 segment.

The further analysis of the hemodynamics in the IA has shown differences that exceed expectations, comparable to those seen in simulation challenges [8,9,11]. The *Simplified* strategy lacks physical reasoning since all of the patient geometries in this study exhibit PCom arteries. Simulations confirm that neglecting these significantly alters the intrasaccular hemodynamics, confirming the initial intuition. Without further exploration of this strategy, we conclude that it is unsuitable for the presented vasculatures.

The *Middle* extension, commonly found in literature, presents more similarities with *Full CoW* simulations. However, moderate changes in hemodynamics sometimes result in magnified alterations in WSS. These differences may lead to varied correlations between flow dynamics and the aneurysm evolution [29]. Causes for these observations included changed boundary flow rates on one side and the lack of interactions with the opposing hemisphere and the posterior circulation on the other.

The additional blood suppliers in the case of *Full* simulations, such as the neighbouring ICA and the BA, are participants in causing blood to traverse communicating vessels into other circulation segments. Although most of the interhemispheric flow was observed at the ACom, hence distal to the aneurysm fundus, the influence of the inflow streams cannot be generally disregarded from being important [22]. In our study, equal flow rates for the ICAs were imposed, aligning with a popular choice shown in [8] due to a lack of measurement data. As stated before, this is irrefutably one of the biases taken into consideration that could be lifted by measurements in follow-up work. The second factor causing altered results between the *Full CoW* and *Middle* simulations is, as stated, the interaction between both anterior and posterior circulations. By not imposing a boundary midway in a posterior communicating artery, more slack is left for the flow to unravel its natural characteristics thereby providing a more physiological hemodynamic profile. Examples of this, among others, are pressure drops at posterior arterial junctions and bifurcations that effectively alter upstream pressure distributions and are of notable relevance [15,48].

The flow in these communicating vessels holds significant medical importance, given that 60-70% of all IAs are located on the Circle of Willis, which itself constitutes 85% of all IAs [49]. These vessels are both abundant and intricate, often presenting challenges in treatment due to their small size, contributing substantially to the incidence of ruptures [50]. While the role of CFD in diagnosing and analyzing IA growth and remodeling processes remains uncertain, it is crucial to acknowledge that modeling choices significantly impact the hemodynamics of communicating vessels [51]. Moreover, statistical evidence indicates that the absence or hypoplasia of certain communicating segments is associated with a higher likelihood of developing IAs [52,53]. As such, it becomes imperative to continually evaluate and refine CFD models to capture the hemodynamics of the CoW more effectively. This ongoing consideration is essential for advancing research and addressing the multitude of unanswered questions surrounding intracranial aneurysms.

5. Conclusion

In this study, we conducted a detailed analysis of how different domain extensions and complexity levels affect hemodynamics in the brain's Circle of Willis. Using patient-specific

geometries and computational fluid dynamics, we simulated three models of increasing complexity inspired by common literature findings for each patient. All these simulations considered non-Newtonian, pulsatile fluid flow, and outflow splits were determined using Murray's law.

The obtained results showed notable variations in flow patterns throughout the arterial network, particularly in two out of the three cases. This highlights the importance of carefully analyzing topology to avoid modelling errors and conflicting results.

We conclude that for an analysis of hemodynamic risk indicators, studying the patient-specific Circle of Willis anatomy or utilizing measurement data is important to ensure physiological hemodynamics. To balance computational demands and accuracy, we suggest a two-step approach: a coarse large-scale simulation of the CoW to provide boundary conditions and a highly resolved local simulation focused on the region of interest, ensuring both reliability and high-fidelity hemodynamics. This approach can be applied to other vascular pathologies as well.

This study deals with the modelling challenge in IA research, which, if addressed comprehensively, could reduce discrepancies in computational fluid dynamics results, enhancing our understanding of IAs and their treatment principles.

Conflict of Interests

On behalf of all authors, the corresponding author states that there is no conflict of interest.

Author Contributions: Conceptualization, P. Jeken-Rico. and A. Goetz.; methodology, P. Jeken-Rico.; software, A. Larcher.; validation, P. Jeken-Rico., P. Meliga. and A. Goetz.; formal analysis, P. Jeken-Rico.; investigation, P. Jeken-Rico.; resources, Y. Özpeynirci.; data curation, Y.Özpeynirci.; writing—original draft preparation, P. Jeken-Rico.; writing—review and editing, A. Goetz.; P. Meliga.; visualization, A. Goetz.; supervision, E.Hachem.; project administration, E.Hachem; funding acquisition, E.Hachem. All authors have read and agreed to the published version of the manuscript.

Funding: This research was funded by the Horizon ERC (European Union) grant number 101045042, Project CURE. Views and opinions expressed are however those of the authors only and do not necessarily reflect those of the European Union or the European Research Council Executive Agency. Neither the European Union nor the granting authority can be held responsible for them. Parts of this research were carried within the European Union's Horizon 2020 research and innovation programme under the Marie Skłodowska-Curie grant agreement No 945304 - Cofund AI4theSciences hosted by PSL University.

Informed Consent Statement: Specific patient consent was waived due to the retrospective study design.

Conflicts of Interest: The authors declare no conflict of interest.

Abbreviations

The following abbreviations are used in this manuscript:

IA	Intracranial Aneurysm	MCA	Middle Cerebral Artery
CFD	Computational Fluid Dynamics	PCA	Posterior Cerebral Artery
CoW	Circle of Willis	ACA	Anterior Cerebral Artery
WSS	Wall Shear Stress	ACom	Anterior Communicating Artery
OSI	Oscillatory Shear Index	PCom	Posterior Communicating Artery
ICA	Internal Carotid Artery		

References

1. Wójtowicz, K.; Przepiorka, L.; Kujawski, S.; Marchel, A.; Kunert, P. Unruptured Anterior Communicating Artery Aneurysms: Management Strategy and Results of a Single-Center Experience. *Journal of Clinical Medicine* **2023**, *12*. <https://doi.org/10.3390/jcm12144619>.
2. Juvela, S. Outcome of Patients with Multiple Intracranial Aneurysms after Subarachnoid Hemorrhage and Future Risk of Rupture of Unruptured Aneurysm. *Journal of Clinical Medicine* **2021**, *10*. <https://doi.org/10.3390/jcm10081712>.

3. Pagiola, I.; Mihalea, C.; Caroff, J.; Ikka, L.; Chalumeau, V.; Iacobucci, M.; Ozanne, A.; Gallas, S.; Marques, M.; Nalli, D.; et al. The PHASES score: To treat or not to treat? Retrospective evaluation of the risk of rupture of intracranial aneurysms in patients with aneurysmal subarachnoid hemorrhage. *Journal of Neuroradiology* **2020**. <https://doi.org/10.1016/j.neurad.2019.06.003>. 354-356
4. Cebal, J.R.; Mut, F.; Raschi, M.; Scrivano, E.; Ceratto, R.; Lylyk, P.; Putman, C.M. Aneurysm rupture following treatment with flow-diverting stents: Computational hemodynamics analysis of treatment. *American Journal of Neuroradiology* **2011**, *32*, 27–33. <https://doi.org/10.3174/ajnr.A2398>. 357-359
5. Janiga, G.; Berg, P.; Sugiyama, S.; Kono, K.; Steinman, D.A. The computational fluid dynamics rupture challenge 2013 - Phase I: Prediction of rupture status in intracranial aneurysms. *American Journal of Neuroradiology* **2015**. <https://doi.org/10.3174/ajnr.A4157>. 360-362
6. Berg, P.; Roloff, C.; Beuing, O.; Voß, S.; Sugiyama, S.; Aristokleous, N.; Anayiotos, A.S.; Ashton, N.; Revell, A.; Bressloff, N.W.; et al. The Computational Fluid Dynamics Rupture Challenge 2013 - Phase II: Variability of Hemodynamic Simulations in Two Intracranial Aneurysms. *Journal of Biomechanical Engineering* **2015**. <https://doi.org/10.1115/1.4031794>. 363-365
7. Voß, S.; Glaßer, S.; Hoffmann, T.; Beuing, O.; Weigand, S.; Jachau, K.; Preim, B.; Thévenin, D.; Janiga, G.; Berg, P. Fluid-Structure Simulations of a Ruptured Intracranial Aneurysm: Constant versus Patient-Specific Wall Thickness. *Computational and Mathematical Methods in Medicine* **2016**, *2016*. <https://doi.org/10.1155/2016/9854539>. 366-368
8. Valen-Sendstad, K.; Bergersen, A.W.; Shimogonya, Y.; Goubergrits, L.; Bruening, J.; Pallares, J.; Cito, S.; Piskin, S.; Pekkan, K.; Geers, A.J.; et al. Real-World Variability in the Prediction of Intracranial Aneurysm Wall Shear Stress: The 2015 International Aneurysm CFD Challenge. *Cardiovascular Engineering and Technology* **2018**. <https://doi.org/10.1007/s13239-018-00374-2>. 369-371
9. Berg, P.; Voß, S.; Saalfeld, S.; Janiga, G.; Bergersen, A.; Valen-Sendstad, K.; Bruening, J.; Goubergrits, L.; Spuler, A.; Cancelliere, N.; et al. Multiple Aneurysms AnaTomy CHallenge 2018 (MATCH): Phase I: Segmentation. *Cardiovascular Engineering and Technology* **2018**. <https://doi.org/10.1007/s13239-018-00376-0>. 372-374
10. Voß, S.; Beuing, O.; Janiga, G.; Berg, P. Multiple Aneurysms AnaTomy CHallenge 2018 (MATCH)-Phase Ib: Effect of morphology on hemodynamics. *PLOS ONE* **2019**. <https://doi.org/10.1371/journal.pone.0216813>. 375-376
11. Berg, P.; Voß, S.; Janiga, G.; Saalfeld, S.; Bergersen, A.W.; Valen-Sendstad, K.; Bruening, J.; Goubergrits, L.; Spuler, A.; Chiu, T.L.; et al. Multiple Aneurysms AnaTomy CHallenge 2018 (MATCH)—phase II: rupture risk assessment. *International Journal of Computer Assisted Radiology and Surgery* **2019**. <https://doi.org/10.1007/s11548-019-01986-2>. 377-379
12. Berg, P.; Saalfeld, S.; Voß, S.; Beuing, O.; Janiga, G. A review on the reliability of hemodynamic modeling in intracranial aneurysms: Why computational fluid dynamics alone cannot solve the equation. *Neurosurgical Focus* **2019**. <https://doi.org/10.3171/2019.4.FOCUS19181>. 380-382
13. Marsden, A.L.; Feinstein, J.A.; Taylor, C.A. A computational framework for derivative-free optimization of cardiovascular geometries. *Computer Methods in Applied Mechanics and Engineering* **2008**, *197*, 1890–1905. <https://doi.org/10.1016/j.cma.2007.12.009>. 383-385
14. Helthuis, J.H.; van Doormaal, T.P.; Hillen, B.; Bleys, R.L.; Hartevelde, A.A.; Hendrikse, J.; van der Toorn, A.; Brozici, M.; Zwanenburg, J.J.; van der Zwan, A. Branching Pattern of the Cerebral Arterial Tree. *Anatomical Record* **2019**. <https://doi.org/10.1002/ar.23994>. 386-388
15. Chnafa, C.; Valen-Sendstad, K.; Brina, O.; Pereira, V.M.; Steinman, D.A. Improved reduced-order modelling of cerebrovascular flow distribution by accounting for arterial bifurcation pressure drops. *Journal of Biomechanics* **2017**. <https://doi.org/10.1016/j.jbiomech.2016.12.004>. 389-391
16. Saalfeld, S.; Voß, S.; Beuing, O.; Preim, B.; Berg, P. Flow-splitting-based computation of outlet boundary conditions for improved cerebrovascular simulation in multiple intracranial aneurysms. *International Journal of Computer Assisted Radiology and Surgery* **2019**. <https://doi.org/10.1007/s11548-019-02036-7>. 392-394
17. Rosner, J.; Reddy, V.; Lui, F. *Neuroanatomy, Circle of Willis*, 1 ed.; StatPearls Publishing, 2022. 395
18. Devault, K.; Gremaud, P.A.; Novak, V.; Olufsen, M.S.; Vernières, G.; Peng, Z. Blood Flow in the Circle of Willis: Modelling and Calibration. *PMC* **2008**. <https://doi.org/10.1016/j.trsl.2012.08.005>. 396-397
19. Malm, J.; Birnefeld, J.; Zarrinkoob, L.; Wählin, A.; Eklund, A. Hemodynamic Disturbances in Posterior Circulation Stroke: 4D Flow Magnetic Resonance Imaging Added to Computed Tomography Angiography. *Frontiers in Neuroscience* **2021**. <https://doi.org/10.3389/fnins.2021.656769>. 400
20. Hindenes, L.B.; Håberg, A.K.; Johnsen, L.H.; Mathiesen, E.B.; Robben, D.; Vangberg, T.R. Variations in the circle of willis in a large population sample using 3D TOF angiography: The tromsø study. *PLoS ONE* **2020**. <https://doi.org/10.1371/journal.pone.0241373>. 401-403
21. Chnafa, C.; Brina, O.; Pereira, V.M.; Steinman, D.A. Better Than Nothing: A Rational Approach for Minimizing the Impact of Outflow Strategy on Cerebrovascular Simulations. *American Journal of Neuroradiology* **2018**. <https://doi.org/10.3174/ajnr.A5484>. 404-405
22. Castro, M.; Putman, C.; Cebal, J. Computational Fluid Dynamics Modeling of Intracranial Aneurysms: Effects of Parent Artery Segmentation on Intra-Aneurysmal Hemodynamics. *American Journal of Neuroradiology* **2006**, *27*, 1703–1709, [<http://www.ajnr.org/content/27/8/1703.full.pdf>]. 406-408
23. Dennis, K.D.; Kallmes, D.F.; Dragomir-Daescu, D. Cerebral aneurysm blood flow simulations are sensitive to basic solver settings. *Journal of Biomechanics* **2017**. <https://doi.org/10.1016/j.jbiomech.2017.03.020>. 409-410
24. Britz, G.; Golshani, K.; Ferrell, A.; Zomorodi, A.; Smith, T. A review of the management of posterior communicating artery aneurysms in the modern era. *Surgical Neurology International* **2010**. <https://doi.org/10.4103/2152-7806.74147>. 411-412

25. Geuzaine, C.; Remacle, J.F. Gmsh: A 3-D Finite Element Mesh Generator with built-in Pre- and Post-Processing Facilities. *International Journal for Numerical Methods in Engineering* **2009**. <https://doi.org/10.1002/nme.2579>. 413
26. Hachem, E.; Rivaux, B.; Kloczko, T.; Digonnet, H.; Coupez, T. Stabilized finite element method for incompressible flows with high Reynolds number. *Journal of Computational Physics* **2010**. <https://doi.org/10.1016/j.jcp.2010.07.030>. 414
27. Coupez, T.; Hachem, E. Solution of high-Reynolds incompressible flow with stabilized finite element and adaptive anisotropic meshing. *Computer Methods in Applied Mechanics and Engineering* **2013**. <https://doi.org/10.1016/j.cma.2013.08.004>. 415
28. Meliga, P.; Hachem, E. Time-accurate calculation and bifurcation analysis of the incompressible flow over a square cavity using variational multiscale modeling. *Journal of Computational Physics* **2019**, *376*, 952–972. <https://doi.org/10.1016/j.jcp.2018.09.036>. 416
29. Valen-Sendstad, K.; Steinman, D.A. Mind the gap: Impact of computational fluid dynamics solution strategy on prediction of intracranial aneurysm hemodynamics and rupture status indicators. *American Journal of Neuroradiology* **2014**, *35*, 536–543. <https://doi.org/10.3174/ajnr.A3793>. 417
30. Goetz, A.; Rico, P.J.; Chau, Y.; Sédat, J.; Larcher, A.; Hachem, E. Proposal for Numerical Benchmarking of Fluid-Structure Interaction in Cerebral Aneurysms. *Preprint* **2023**, pp. 1–23, [2308.08301]. <https://doi.org/10.48550/arXiv.2308.08301>. 418
31. Hodis, S.; Uthamaraj, S.; Smith, A.L.; Dennis, K.D.; Kallmes, D.F.; Dragomir-Daescu, D. Grid convergence errors in hemodynamic solution of patient-specific cerebral aneurysms. *Journal of Biomechanics* **2012**, *45*, 2907–2913. <https://doi.org/10.1016/j.jbiomech.2012.07.030>. 419
32. Abraham, F.; Behr, M.; Heinkenschloss, M. Shape optimization in unsteady blood flow: A numerical study of non-Newtonian effects. *Computer Methods in Biomechanics and Biomedical Engineering* **2005**. <https://doi.org/10.1080/10255840500309562>. 420
33. Xiang, J.; Tremmel, M.; Kolega, J.; Levy, E.I.; Natarajan, S.K.; Meng, H. Newtonian viscosity model could overestimate wall shear stress in intracranial aneurysm domes and underestimate rupture risk. *Journal of NeuroInterventional Surgery* **2012**, *4*, 351–357. <https://doi.org/10.1136/neurintsurg-2011-010089>. 421
34. Gambaruto, A.M.; Janela, J.; Moura, A.; Sequeira, A. Sensitivity of hemodynamics in a patient specific cerebral aneurysm to vascular geometry and blood rheology. *Mathematical Biosciences and Engineering* **2011**. <https://doi.org/10.3934/mbe.2011.8.409>. 422
35. Tanaka, H.; Fujita, N.; Enoki, T.; Matsumoto, K.; Watanabe, Y.; Murase, K.; Nakamura, H. Relationship between Variations in the Circle of Willis and Flow Rates in Internal Carotid and Basilar Arteries Determined by Means of Magnetic Resonance Imaging with Semiautomated Lumen Segmentation: Reference Data from 125 Healthy Volunteers. *AJNR Am J Neuroradiol* **2006**, *27*, 1770–1775. 423
36. Vignon-Clementel, I.E.; Alberto Figueroa, C.; Jansen, K.E.; Taylor, C.A. Outflow boundary conditions for three-dimensional finite element modeling of blood flow and pressure in arteries. *Computer Methods in Applied Mechanics and Engineering* **2006**. <https://doi.org/10.1016/j.cma.2005.04.014>. 424
37. Janiga, G.; Berg, P.; Beuing, O.; Neugebauer, M.; Gasteiger, R.; Preim, B.; Rose, G.; Skalej, M.; Thevenin, D. Recommendations for accurate numerical blood flow simulations of stented intracranial aneurysms. *Biomedizinische Technik* **2013**, *58*, 303–314. <https://doi.org/10.1515/bmt-2012-0119>. 425
38. Bousset, L.; Rayz, V.L.; McCulloch, C.; Martin, A.; Acevedo-Bolton, G.; Lawton, M.; Higashida, R.; Smith, W.S.; Young, W.L.; Saloner, D. Aneurysm growth occurs at region of low wall shear stress: Patient-specific correlation of hemodynamics and growth in a longitudinal study. *Stroke* **2008**. <https://doi.org/10.1161/STROKEAHA.108.521617>. 426
39. Urschel, K.; Tauchi, M.; Achenbach, S.; Dietel, B. Investigation of wall shear stress in cardiovascular research and in clinical practice—from bench to bedside. *International Journal of Molecular Sciences* **2021**. <https://doi.org/10.3390/ijms22115635>. 427
40. Cebal, J.; Detmer, F.; Chung, B.; Choque-Velasquez, J.; Rezai Jahromi, B.; Lehto, H.; Tulamo, R.; Hernesniemi, J.; Niemela, M.; Yu, A.; et al. Local Hemodynamic Conditions Associated with Focal Changes in the Intracranial Aneurysm Wall. *AJNR. American journal of neuroradiology* **2019**, *40*, 510–516. <https://doi.org/10.3174/ajnr.A5970>. 428
41. Meng, H.; Tutino, V.M.; Xiang, J.; Siddiqui, A. High WSS or Low WSS? Complex interactions of hemodynamics with intracranial aneurysm initiation, growth, and rupture: Toward a unifying hypothesis. *AJNR* **2014**. <https://doi.org/10.3174/ajnr.A3558>. 429
42. Malek, A. Hemodynamic Shear Stress and Its Role in Atherosclerosis. *JAMA* **1999**, *282*, 2035. <https://doi.org/10.1001/jama.282.21.2035>. 430
43. Furukawa, K.; Ishida, F.; Tsuji, M.; Miura, Y.; Kishimoto, T.; Shiba, M.; Tanemura, H.; Umeda, Y.; Sano, T.; Yasuda, R.; et al. Hemodynamic characteristics of hyperplastic remodeling lesions in cerebral aneurysms. *PLOS ONE* **2018**, *13*, 1–11. <https://doi.org/10.1371/journal.pone.0191287>. 431
44. Mazzi, V.; Gallo, D.; Calò, K.; Najafi, M.; Khan, M.O.; De Nisco, G.; Steinman, D.A.; Morbiducci, U. A Eulerian method to analyze wall shear stress fixed points and manifolds in cardiovascular flows. *Biomechanics and Modeling in Mechanobiology* **2020**, *19*, 1403–1423. <https://doi.org/10.1007/s10237-019-01278-3>. 432
45. Sheikh, M.A.A.; Shuib, A.S.; Mohyi, M.H.H. A review of hemodynamic parameters in cerebral aneurysm. *Interdisciplinary Neurosurgery: Advanced Techniques and Case Management* **2020**, *22*, 100716. <https://doi.org/10.1016/j.inat.2020.100716>. 433
46. Jongen, J.C.; Franke, C.L.; Ramos, L.M.; Wilminck, J.T.; Van Gijn, J. Direction of Flow in Posterior Communicating Artery on Magnetic Resonance Angiography in Patients with Occipital Lobe Infarcts. *Stroke* **2004**. <https://doi.org/10.1161/01.STR.0000106772.87186.C7>. 434
47. Zarrinkoob, L.; Ambarki, K.; Wählin, A.; Birgander, R.; Eklund, A.; Malm, J. Blood flow distribution in cerebral arteries. *Journal of Cerebral Blood Flow and Metabolism* **2015**, *35*, 648–654. <https://doi.org/10.1038/jcbfm.2014.241>. 435

48. Mynard, J.P.; Valen-Sendstad, K. A unified method for estimating pressure losses at vascular. *International Journal for Numerical Methods in Biomedical Engineering* **2015**. <https://doi.org/10.1002/cnm.2717>. 471
49. Hacein-Bey, L.; Provenzale, J.M. Current Imaging Assessment and Treatment of Intracranial Aneurysms. *American Journal of Roentgenology* **2011**, *196*, 32–44, [<https://doi.org/10.2214/AJR.10.5329>]. PMID: 21178044, <https://doi.org/10.2214/AJR.10.5329>. 472
50. Chen, J.; Li, M.; Zhu, X.; Chen, Y.; Zhang, C.; Shi, W.; Chen, Q.; Wang, Y. Anterior Communicating Artery Aneurysms: Anatomical Considerations and Microsurgical Strategies. *Frontiers in Neurology* **2020**, *11*, 1–15. <https://doi.org/10.3389/fneur.2020.01020>. 473
51. Zhang, H.; Fujiwara, N.; Kobayashi, M.; Yamada, S.; Liang, F.; Takagi, S.; Oshima, M. Development of a Numerical Method for Patient-Specific Cerebral Circulation Using 1D–0D Simulation of the Entire Cardiovascular System with SPECT Data. *Annals of Biomedical Engineering* **2016**, *44*, 2351–2363. <https://doi.org/10.1007/s10439-015-1544-8>. 474
52. Hindenes, L.B.; Ingebrigtsen, T.; Isaksen, J.G.; Håberg, A.K.; Johnsen, L.H.; Herder, M.; Mathiesen, E.B.; Vangberg, T.R. Anatomical variations in the circle of Willis are associated with increased odds of intracranial aneurysms: The Tromsø study. *Journal of the Neurological Sciences* **2023**, *452*. <https://doi.org/10.1016/j.jns.2023.120740>. 475
53. Feng, L.; Mao, H.J.; Zhang, D.D.; Zhu, Y.C.; Han, F. Anatomical variations in the Circle of Willis and the formation and rupture of intracranial aneurysms: A systematic review and meta-analysis. *Frontiers in Neurology* **2023**, *13*. <https://doi.org/10.3389/fneur.2022.1098950>. 476

Disclaimer/Publisher’s Note: The statements, opinions and data contained in all publications are solely those of the individual author(s) and contributor(s) and not of MDPI and/or the editor(s). MDPI and/or the editor(s) disclaim responsibility for any injury to people or property resulting from any ideas, methods, instructions or products referred to in the content. 477